RSC Applied Polymers

ROYAL SOCIETY OF CHEMISTRY

PAPER

View Article Online
View Journal | View Issue

Cite this: *RSC Appl. Polym.*, 2024, **2**, 105

Role of polymer interactions in core–shell filaments in the mechanical properties of 3D printed objects†

Jia-Ruey Ai,[a] Seokhoon Jang,[a] Wyatt Fink,[b] Seong H. Kim[a] and Bryan D. Vogt *[a]

Multi-component structured filaments offer the potential for enhanced mechanical performance in 3D printed plastics. Here, the interactions between filament components in the core (polycarbonate, PC)–shell (polypropylene, PP) geometry are manipulated by light maleation (1%) of PP to understand how the inclusion of favorable polar interactions and potential grafting reactions at the core–shell interface impact the mechanical performance of the 3D printed parts. The elastic modulus of the 3D printed tensile bars is essentially independent of the shell selection for the fully isotactic PP (iPP) or maleated PP (miPP), but the strain at break is generally significantly improved with the miPP shell to increase the toughness of the printed parts for both flat and stand-on build orientations. This is counter to compression molded specimens where iPP is more ductile than miPP. The mechanical behavior in the flat orientation is consistent with long fiber composites, where the PC core essentially acts as fiber-reinforcement. Tribo-testing results indicate increased friction between miPP and PC through the interaction of the maleate anhydride group with the carbonate relative to the iPP with PC. This small increase in the interfacial interaction between the core and shell polymers with miPP increases the work required to pull out fibers of the stiffer PC from the PP matrix for the flat build orientation and more energy is required to delaminate the core from the shell, which is the loci of failure, when the stand-on build orientation is stretched. The subtle change in chemistry with a maleation of 1% of PP leads to a larger strain at failure and tougher parts due to the interaction with PC. These results illustrate that the selection of the polymers in structured filaments needs to also consider their potential intermolecular interactions including the potential for grafting reactions to best enhance the mechanical response of 3D printed parts.

Received 16th September 2023,
Accepted 2nd January 2024

DOI: 10.1039/d3lp00168g

rsc.li/rscapplpolym

Introduction

The advantages of mass customization, lack of tooling requirements, and increased material utilization are typically cited as game-changers for manufacturing enabled by 3D printing,[1] but the mechanical performance of 3D printed plastics tends to limit adaptation of additive manufacturing (AM).[2–4] These mechanical limitations tend to be particularly acute for material extrusion additive manufacturing (MEAM),[5,6] which includes filament-based fabrication that is compatible with a wide range of high performance engineering thermoplastics.[1] These shortcomings in mechanical performance are commonly attributed to the incomplete development of the interface between printed beads or roads[7] due to the highly transient nature of the printing process.[8] Optimization of the printing process tends to fail to achieve the intrinsic mechanical properties of the plastic with significant anisotropy.[9,10] This anisotropy is associated with the differences in the process history and strength between a continuous bead and the interface between printed beads. A variety of post-processing strategies have been employed to work to strengthen the interfaces to improve the properties.[11–13] However, these tend to only marginally improve the properties of the printed parts as the temperatures required to enable chain rearrangements tend to lead to significant flow to deform the printed part,[5,14,15] except in some cases for semicrystalline polymers where annealing between the melting and crystallization temperatures can sometimes lead to improvements in mechanical performance.[13,16] One notable exception is microwave processing of objects printed with carbon nanotube coated filaments,

[a]*Department of Chemical Engineering, The Pennsylvania State University, University Park, PA 16802, USA. E-mail: bdv5051@psu.edu*
[b]*Department of Engineering Science, The Pennsylvania State University, University Park, PA 16802, USA*

†Electronic supplementary information (ESI) available: Additional experimental details and data, including a schematic of coextrusion for filament fabrication, DSC thermograms, mold design for tribology measurements, optical micrographs of the surface of printed objects, surface topology scans, stress–strain curves, and images of fractured tensile bars. See DOI: **https://doi.org/10.1039/d3lp00168g**

where the extra heating is localized to the interfaces.[17] As the mechanical properties of printed plastic parts can be effectively predicted from polymer weld theory,[18] these microwave post-processing results further illustrate that changes to the interfaces between printed beads are critical to improvements with post-processing.

An alternative route to enhance the properties of the interfaces between printed beads is to introduce crosslinks between the printed layers during printing.[6] This leads to more isotropic properties of the printed part than those typically obtained with MEAM, but requires modifications to the printer and print process flow. Instead of covalent crosslinks, transient interactions associated with hydrogen bonding[19] can also be used to improve the interfaces between printed beads without requiring large scale polymer diffusion needed to form entanglements. Nanoparticles are known to enhance adhesion generally[20,21] and nanoparticle modified filaments provide significantly increased strength and higher modulus of 3D printed parts.[22] However, the mechanical properties in the '*z*' direction were not determined. An alternative route to improve the properties through engineering of the filaments involves structuring of polymers within the filament to provide enhanced flow at the surface of the filament, while the center rapidly becomes rigid to provide structural stability to the printed object.[23–27] These structured filaments have most commonly been presented in terms of core–shell geometries,[23–26] where a lower T_g polymer comprises the shell to enable improved formation of the interface between printed beads. Recent work has demonstrated a custom hotend die that can print core–shell structures from two commercial plastic filaments.[28] This core–shell approach also enabled printing highly filled plastics where the shell is unfilled to provide higher mobility for interface development.[29] Numerical simulations have been used to provide physical insights into process control for printing core–shell materials with MEAM.[30] More complex geometries have been demonstrated using active mixing[31] and custom dies.[27] Post-print annealing of these structured filaments provides an opportunity to overcome the typical trade-off between dimensional accuracy and mechanical properties.[27] However the variety of polymers used in these filaments have been generally immiscible, and this structuring of the filaments produces an additional interface within the printed part that arises from the two components within the filament. The role of the interaction between the core and shell polymers in the mechanical performance has not been examined in detail. For core–shell filaments, this interface has been shown to be effectively weak for most examined polymer pairs to lead to effective crack propagation along the core-shell interface when stresses are applied in the '*z*' direction.[25]

In this work, the role of the interactions between the polymers in core–shell filaments on the mechanical properties of 3D printed parts is investigated experimentally while printing in flat (*XY*) and stand-on (*YZ*) build orientations. The goal of this work is to provide an understanding of how the adhesion between the core and shell polymers in these filaments impacts the performance of 3D printed parts to provide guidance for the selection of polymers in multi-component filaments. Here, a polycarbonate (PC) core and a polypropylene (PP) shell enable this investigation where the interaction between materials can be modestly impacted by maleation of PP (miPP). This change does not significantly impact the temperature for solidification of the shell material to provide a direct comparison. Maleation is known to improve the compatibility of polymer blends[32] to improve their mechanical performance,[33] including PC and PP where PC can be grafted to PP through maleic anhydride.[34] Maleation improves the compatibility of PP with more polar polymers, such as poly(vinyl alcohol),[35] typically through grafting with alcohols or amines that decreases the size of the phase segregated domains. The effect of maleation of polyolefins on 3D printed parts has not been investigated. Here, we quantify the influence of maleation (1 mol% of PP) on the adhesion between PC and PP *via* tribology measurements to rationalize differences in the mechanical performance of 3D printed objects using iPP or miPP shells in PC core–shell filaments. The insights gained from this work provide additional concepts for the design of multiple component structured filaments to enhance the toughness of 3D printed parts through polar interactions (maleic anhydride and carbonate).

Experimental section

Materials and filament fabrication

Bisphenol-A polycarbonate (PC, Makrolon 3208) was obtained from Covestro, LLC. Isotactic polypropylene (iPP, PP4792E1) was obtained from ExxonMobil. Maleated polypropylene (miPP, Admer QF580) was obtained from Mitsui Chemical, Inc. The extent of maleation was approximately 1 mol%. The difference in the chemistry of the as-received iPP and miPP can be ascertained from their FTIR spectra (Fig. S1†).[36] Prior to any processing, the polymer pellets were dried under vacuum (−30 in. Hg) for >12 h at 120 °C for PC or 100 °C for iPP and miPP to remove residual moisture. The dried polymer pellets were fabricated into filaments using extrusion. Single component filaments were produced using a HAAKE single-screw extruder (model Rheomex 252p) with a gear pump and a 2.2 mm diameter circular die. The experimental setup for core–shell filament production is schematically illustrated in Fig. S2.† The diameter was decreased to approximately 1.75 mm through drawing using a take-up wheel. The extruded filaments were quenched in a room-temperature water bath prior to winding on the spool. The core–shell structured filaments were fabricated in a similar process but using two single-screw extruders (Rheomex 252p and Akron Extruder M-PAK 150) and a 2 mm co-extrusion die. The detailed setup and extrusion temperature can be found in Fig. S2 in the ESI.† The relative extrusion rates were maintained with melt pumps to produce filaments containing approximately 50 vol% PC. The actual composition of the filaments was determined from

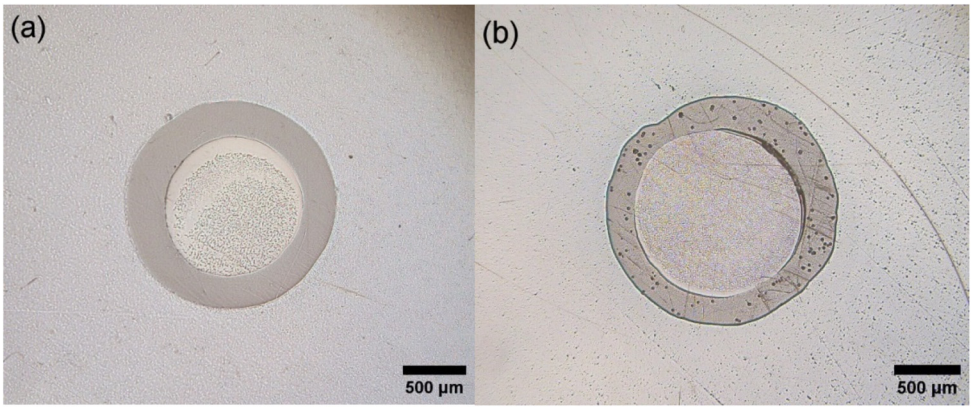

Fig. 1 Optical micrographs of cross-sections of the core–shell filaments. The core ratio is (a) 44.3% for PC-iPP and (b) 49.2% for PC-miPP for these images.

the optical characterization of the cross section of the core–shell filaments as shown in Fig. 1. The PC-iPP and PC-miPP filaments contain 43.7 ± 0.67 vol% and 50.1 ± 0.89 vol% PC, respectively.

The thermal properties were examined by Differential Scanning Calorimetry (DSC, TA Instruments Q2000). Thermograms were obtained under N_2 with a flow rate of 50 ml min^{-1} to determine the processing conditions for the core–shell structured filaments. The resin samples (4–6 mg) were placed in an aluminum DSC pan (DSC Consumables, Inc.) and then hermetically sealed. The thermograms were recorded between 40 °C and 240 °C upon heating and cooling at 10 °C min^{-1} for 2 cycles. The first heating cycle removed the thermal history associated with resin manufacture conditions and aging. The thermal properties were reported from the cooling and 2nd heating branch as shown in Fig. S3.†

Specimen printing and compression molded specimen preparation

The filaments were used to print ASTM D638 Type V tensile bars and ISO/ASTM 52902 test objects with a Roboze One +400 Xtreme printer on vacuum mounted PEI (Gizmo Dorks) at 120 °C as the build bed surface. The ASTM tensile specimen (2 mm thick) was sliced using Simplify3D (software, version 4.1.2). The print parameters were 0.2 mm layer height, 0.48 mm extrusion width, 100% infill and 0°/90° alternative rectilinear infill. The specimens were printed in flat (*XY*) and stand-on (*YZ*) build orientations with three samples printed at each orientation in parallel.[37] The print speed was 20 mm s^{-1} for the *XY* orientation and reduced to 10 mm s^{-1} for the *YZ* orientation along with a 5 mm brim to stabilize the specimen from delamination. The core–shell tensile specimens were printed at extrusion temperatures of 260 °C, 280 °C and 300 °C. To better understand the printability of these filaments, the ISO/ASTM 52902 test object was used, printed at 20 mm s^{-1}, 40% infill and an extrusion temperature dependent on the filament (PC 300 °C, iPP 240 °C, iPP/PC 300 °C and miPP/PC 300 °C).

For comparison, tensile specimens of the individual components (PP, iPP and miPP) were prepared by compression molding with a heat press (Carver, model 3912) and an ASTM D638 type V die with 1.5 mm thickness. Prior to compression molding, a release agent (Stoner, silicon out mold release) was applied to the internal surface of the die to enable facile removal. Sufficient polymer was added to the die and a constant force (2200 N), equivalent to ≈1730 MPa, was applied for 5 min. The molding temperature was selected based on the polymer (PC 240 °C, iPP 200 °C and miPP 200 °C). The specimens were allowed to cool for 30 min prior to removal from the mold. Additional iPP and miPP sheets were also prepared with a 1.5 mm square mold (50 mm × 50 mm). PC spherical balls were fabricated with a customized mold (Fig. S3†). The PC pellets were placed in the socket and then molded following the same procedure for the tensile specimen.

Morphological characterization

To quantify the dimensional accuracy performance, a blue light scanning camera (Polyga, HDI-C109) equipped with a rotary stage was used to capture the 3D structure. A checkerboard on a rotary stage was used to calibrate a FlexScan3D camera system (Polyga, version 3.3.12). The specimens were coated (AESUB blue 3D scanning spray, AESUB) and fixed to the rotary stage with nonhardening clay (Sargent Art) prior to the scan. The scan parameters were set to produce a 100% mesh density with an interval spacing of 0.06 and 12 images for each scan. A total of 2 scans were performed for the tensile bars with different locations for the clay to capture the full specimen, while 4 scans were used for the ISO/ASTM 52902 specimens to maximize the resolution of protruded structures. These scans were aligned and combined to produce a single 3D structure. The finalized 3D structures were then compared with the original CAD file within GOM inspect 2019 with the three-point alignment method to produce false color images to illustrate the dimensional accuracy locally with the prints. The surface morphology of the printed objects was characterized using optical profilometry (Zeta-20, NanoScience Instruments).

The profilometry images were analyzed using line cuts to elucidate the amplitude of the periodicity associated with adjacent beads.

Mechanical testing

The rheological characteristics of the polymers were assessed using small angle oscillatory shear (SAOS) measurements with a Discovery HR 20 rheometer (TA Instruments). The samples were dried and then tested in a parallel plate geometry (25 mm diameter) at 240 °C using a 1% strain amplitude. The data were collected over a frequency range from 0.01 to 100 rad s^{-1}.

The tensile properties of the printed specimens were measured using an MTS 50kN load frame system (Criterion model 43) with a 5kN load cell and video extensometer. The tensile tests were performed at 10 mm min^{-1}. This rate is within the recommended crosshead rates for ASTM D638 testing (5–500 mm min^{-1}). The true strain was captured using a video extensometer. For each print condition, a minimum of three specimens were tested. The results are reported as the average with an uncertainty associated with the standard error of the measurement determined by the variance associated with multiple measurements.

Tribo-testing

All friction tests were performed with a custom-designed ball-on-flat reciprocating tribometer under ambient conditions. Before the friction tests, the molded iPP and miPP sheets were washed with soapy water followed by isopropyl alcohol to remove any mold release agent. The clean polymer sheets were blow-dried with compressed air and cut using a razor blade to approximately 1 cm × 1 cm to fit into the tribometer. A 3 mm diameter PC sphere was used as a counter surface to measure friction upon rubbing on the iPP or miPP surface. The spheres were molded using the design shown in Fig. S4.† The applied load was 0.5 N, and the sliding speed was 2.5 mm s^{-1} over a span of 2.5 mm. The tribo-test was performed at room temperature in a dry nitrogen environment.

Results and discussion

Fig. 2 illustrates the differences in the printability of the filaments for the polymers examined in this work. The ASTM/ISO print standard was developed to provide insights into the limits of 3D printing for different material/printer combinations as well as provide system calibration. The features in the test specimen provide a test bed for resolution limits with slot, pin and hole artifacts, overhang angle, and unsupported spans. In general, the same features exhibit similar difficulties across the filaments printed from the examination of the images and the 3D scans. The two thinnest ribs did not print in any of the specimens, which is associated with the resolution limit of the MEAM printer used. There is also some deformation in the unsupported print associated with the rails in the back for the orientation shown in Fig. 2. However, the extent of the deviations in the print does depend on the filament used. As rheology is known to impact the printability of polymers with MEAM, small amplitude oscillatory shear (SAOS) measurements were performed for the 3 base polymers: PC, iPP and miPP. Fig. S5† illustrates the storage and loss moduli of these polymers at 240 °C. At a low shear rate (0.01 rad s^{-1}), the loss moduli of PC and iPP are similar, while the loss modulus of miPP is more than a factor of 3.7 lower. This is consistent with the reported melt flow indices and the complex viscosity at low shear rates. The origin of the difference in viscosity is likely the average molecular weight. The radicals required to graft maleic anhydride to PP results in beta scission and reduction in the average molecular mass,[38] which is consistent with the reduced viscosity. This difference in molecular mass needs to be considered when comparing the core–shell filaments as engineering of the molecular mass

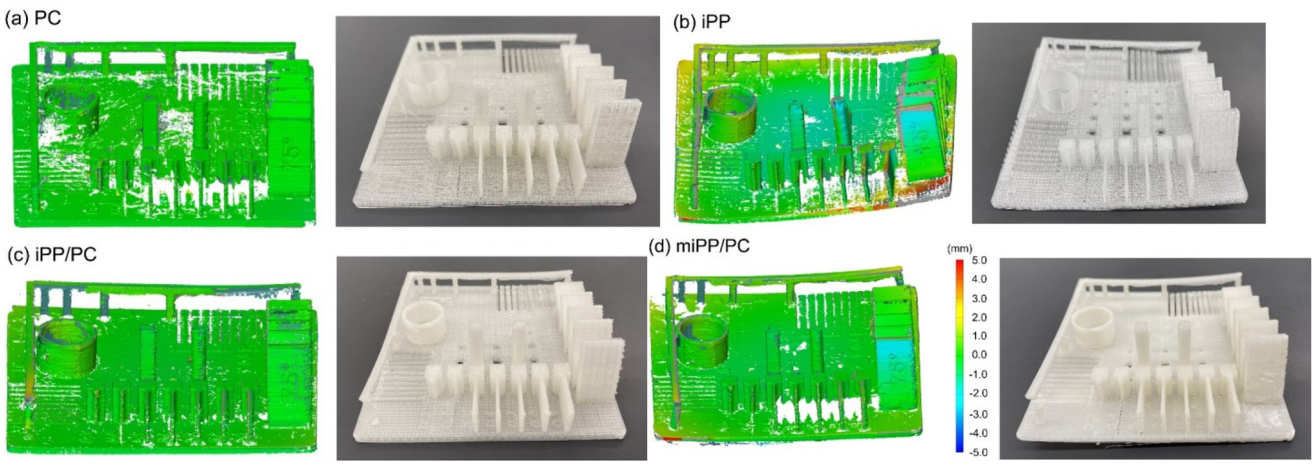

Fig. 2 False color 3D scan and a photograph of the ASTEM/ISO print standard using (a) PC, (b) iPP, (c) iPP/PC shell/core and (d) miPP/PC shell core filaments. The extrusion temperature used for the prints was 300 °C except for iPP, which was printed at 240 °C. The same color map applies to each 3D scan. The areas in white were not resolved by the scans used due to shadowing by other features in the geometries scanned.

distribution impacts the mechanical performance of glassy polymers printed by MEAM.[39]

As shown in Fig. 2a, the combination of a relatively high T_g value, limited volume change upon solidification, and adequate stiffness of the glass for PC leads to good dimensional accuracy overall from the 3D scan. This contrasts with the iPP print (Fig. 2b) where there is clear warpage and bowing of the overall part with the front right and back left corners being bent upwards. Moreover, there is clear deformation of the overhang print at 75° where the upper part of the artifact is thinner than the digital design. This poorer print capability of iPP is not surprising given the reported challenges with printing polypropylene due to its large volume change upon crystallization[40] and the variety of strategies implemented to reduce the deformation.[41–43] Here, the iPP filaments were not formulated to improve the 3D printing performance. For the core–shell filaments that contain approximately $\frac{1}{2}$PC and $\frac{1}{2}$iPP shown in Fig. 2c, the dimensional accuracy is similar to pure PC except for the unsupported print rails where there is some added deformation. Visual inspection of the surface illustrates that the printed lines are not as apparent in the iPP/PC in comparison with the PC. There is some degradation in the dimensional accuracy when switching to miPP with the core–shell filaments (Fig. 2d). This is attributed to the increased flow of miPP as a result of the lower viscosity (Fig. S5†) and its lower modulus in the solid state. As the maleation extent is low (*ca.* 1%), it is not expected to significantly alter the flow at the core–shell interface from interactions between the maleic anhydride in miPP and the carbonyl in PC, although grafting reactions would broaden the interfacial width.

To better quantify differences in the printability of these different filaments, the hole printing in the standard specimens was examined. Fig. 3 illustrates the areal accuracy of the 12 different holes in the test specimens for the different filaments. These holes are associated with three different shapes, circles, squares and hexagons, as well as three nominal sizes (1, 2, 3, 4 mm) for each shape. The images used to calculate the hole areas are shown in Fig. S6.† For circular holes (Fig. 3a), there is good agreement between the model and print with PC for the 3 and 4 mm holes (>98%), while the holes printed with the other filaments tend to be appreciably smaller with ~90% of the area at 4 mm and ~85% of the area of 3 mm. This decreased ability to accurately print holes with polyolefin containing filaments may be associated with their lower surface energy (typically 31–32 mN m^{-1} in comparison with ~40 mN m^{-1} for PC) and the volumetric change upon melting of the PP crystals that leads to an initially larger bead. However decreasing the hole size leads to a significant degradation in the hole accuracy for all of the filaments examined. At 1 mm design, core–shell filaments perform worse than the iPP or PC alone. This difference may be associated with the higher print temperature with the core–shell filaments than for iPP, which provides more opportunity for flow. In particular, the hole printed with the miPP/PC filament is nearly closed. The force for closure of the hole would be surface tension, but the viscosity of the polymer would act to limit the

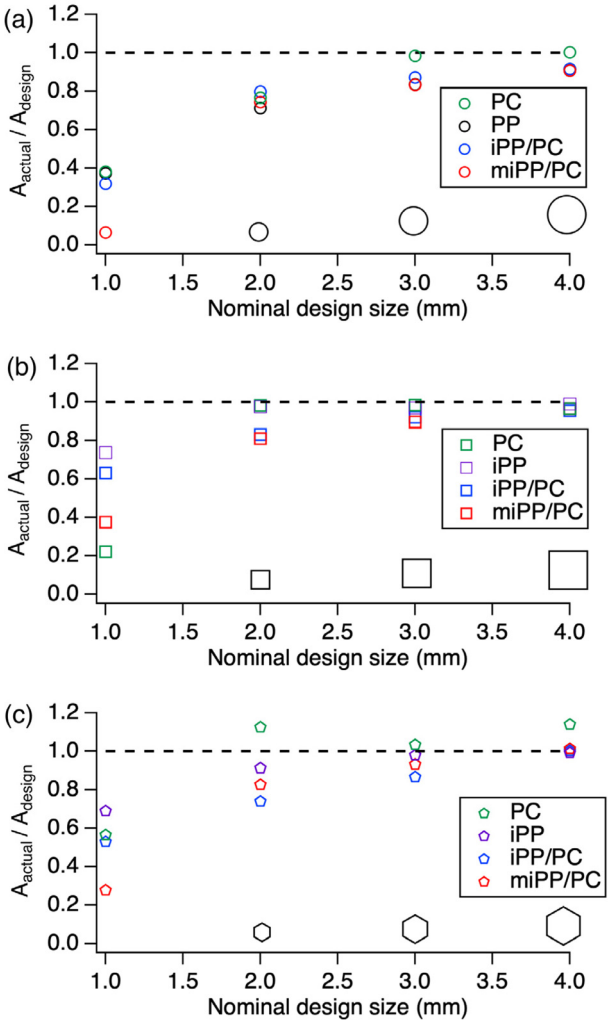

Fig. 3 Relative area of the (a) circular, (b) square and (c) hexagonal holes in the ASTM/ISO print standard using PC, iPP, iPP/PC shell/core and miPP/PC shell core filaments. The area is relative to the CAD design for the print standard.

closure. The higher extrusion temperatures with the core–shell filament increase the time that the shell in the melt can flow. The differences in the hole size between the iPP and miPP shells are likely associated with differences in the viscosity where the melt flow index (MFI) of miPP (7.7 g per 10 min) is nearly 3 times as high as the MFI of iPP (2.7 g per 10 min) from the data sheets for the plastics. This is also consistent with the rheology from the small amplitude oscillatory shear (SAOS) as shown in Fig. S6† where the storage modulus for iPP is approximately double that of miPP at 0.01 rad s^{-1} and 200 °C. These data are consistent with a lower average molecular weight for miPP; reduction in the molecular weight of PP during maleation is common due to simultaneous beta scission occurring with the desired reaction.[44]

Similarly with a square hole (Fig. 3b), the relative accuracy of the hole size decreases as the nominal hole size decreases. However, the iPP filament in general leads to better areal accu-

racy. This difference is likely associated with the print path changes between a circle and a square. The largest effect of the filament selection is observed with the smallest (1 mm) hole, where the miPP/PC filament does not perform as well as the iPP/PC core shell filament. This behavior is consistent across the three hole shapes examined for the 1 mm hole, which points towards the viscosity of the shell being important to maintaining small holes in printed structures especially considering the higher printing temperatures.

As the viscosity difference between miPP and iPP appears to impact the accuracy of printed holes, the surface finish may be impacted by this selection as well. Fig. S7a† illustrates a representative block printed with the two core–shell filaments. Examination of this surface by optical profilometry reveals a periodic surface associated with the layering of the printed beads. Fig. 4 illustrates the surface morphology of the printed core–shell filaments at the different print temperatures examined. Visually the surfaces are similar with clear degradation in the aligned parallel bead structure at 300 °C when using miPP/PC. Although the full optical profilometry scans can quantify the surface morphology through average roughness (R_a), this averaging loses the directionality associated with the print. As the flow of the polymer will reduce the peak to valley amplitude between adjacent beads, examination of the profiles solely in this direction will provide insights into the polymer flow that occurs transversely to the print direction. The R_a value in this case will be predominately influenced by the interbead height variation associated with the print path.

Fig. 5A illustrates the differences in the 1D profiles between miPP and iPP shells when printed at 300 °C. Line cuts are perpendicular to the printed beads at a spacing of 150 mm between cuts. There are 10 curves shown in Fig. 5A for each print condition. The amplitude of the oscillations associated with the printed beads decreases with the use of miPP in the shell. This is consistent with increased flow as might be expected due to the higher MFI and lower viscosity. Analogous tensile test profiles associated with the other print conditions are shown in Fig. S7.† The absolute value of the deviation of the height from the average of these 1D profiles provides a roughness metric (R_a) that is biased to the interbead roughness as opposed to intrinsic roughness along the printed bead. Fig. 5B illustrates this roughness as a function of print temperature for the two filaments. At the lowest temperature printed (260 °C), there is no statistical difference in R_a between iPP and miPP shells; this is somewhat surprising given the lower viscosity for miPP, which should promote additional

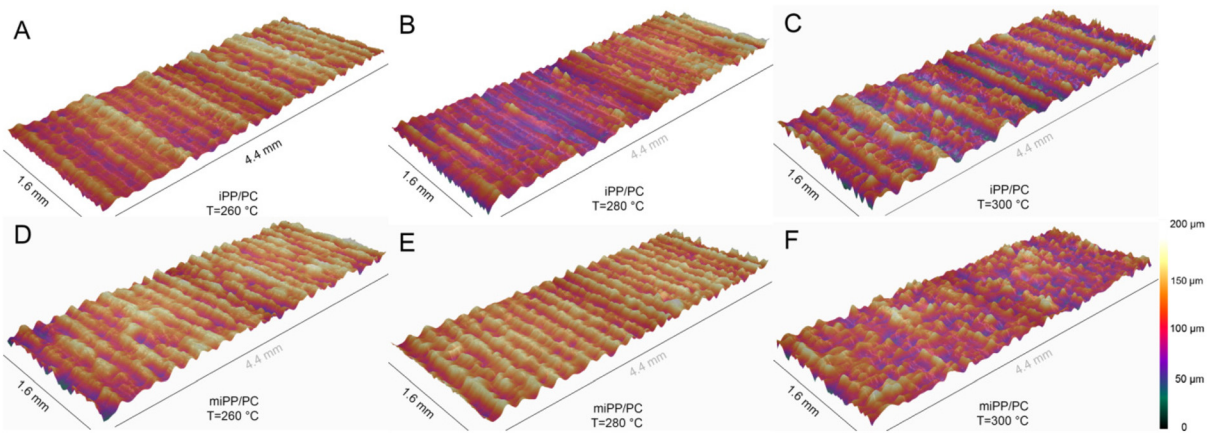

Fig. 4 Optical profilometry surface morphology for iPP/PC printed at (A) 260 °C, (B) 280 °C and (C) 300 °C and miPP/PC printed at (D) 260 °C, (E) 280 °C and (F) 300 °C. The periodic structure associated with the adjacent beads can be readily observed. A common height scale is used for all images.

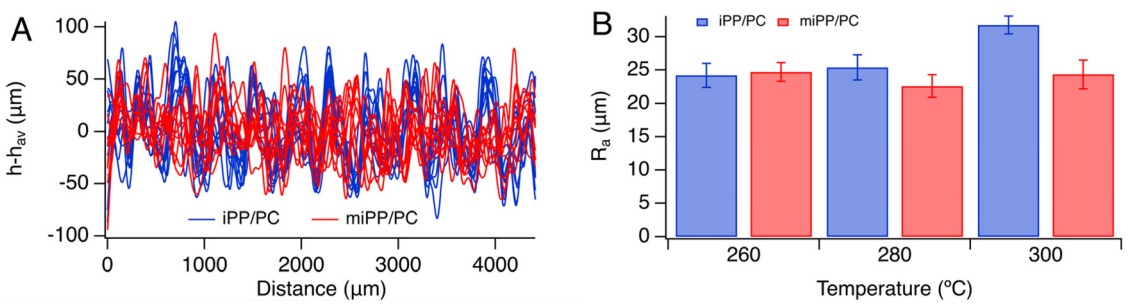

Fig. 5 (A) Line cuts of profilometry data perpendicular to the bead print direction for iPP/PC and miPP/PC materials printed at 300 °C. (B) 1D root mean square roughness obtained from line cuts orthogonal to the bead print direction as a function of the filament and print temperature.

flow. However, rapid cooling during the print likely limits the potential for additional flow. At 280 °C, there is a modest decrease in the average roughness with the miPP shell, while the roughness using the iPP shell is essentially unchanged. This is consistent with the additional flow of miPP due to its lower viscosity to level out the height differences associated with the interbead region. However increasing the temperature to 300 °C leads to an increase in the roughness, most notably for the iPP shell as shown in Fig. 5B. This increase in roughness is counter to expectations that increasing temperature will tend to reduce the interbead roughness. Examination of the 2D profilometry data provides hints of the origins of this increased roughness. There are nodules that appear on the surface of the 300 °C prints (Fig. 4) that are in some cases greater than the peak to valley height between beads. The bead morphology is still clearly distinguishable for the iPP shell, but this is significantly reduced for miPP. Thus, there is a significant increase in roughness with iPP/PC at 300 °C due to the combined effect of the nodules and the interbead morphology. Nonetheless, the similarity in roughness indicates that large scale flow between adjacent beads does not appreciably depend on the melt viscosity of the shell polymer over the short timescales between printing and solidification.

Although the near net shape manufacture, and thus dimensional accuracy, is a key attribute of 3D printing, the performance of plastic parts manufactured by MEAM tends to be limited by their mechanical attributes.[2] Fig. 6 illustrates representative stress–strain responses for the two core–shell materials as a function of build orientation and extrusion temperature. All of the stress–strain curves for the specimens tested are shown in Fig. S8† for iPP/PC and Fig. S9† for miPP/PC core–shell printed tensile specimens. When printed in the flat build orientation (Fig. 6a), the tensile behavior for the miPP/PC and iPP/PC core–shell materials are qualitatively similar for the different extrusion temperatures examined. There is initially a sharp increase in stress up to approximately 10% strain, which is associated with the elastic modulus. The specimens yield and then extend at lower stress to failure. The effect of miPP *versus* iPP in the shell appears to be primarily associated with the post-yield behavior with the miPP/PC material being more ductile for most temperatures examined. This difference can be rationalized in terms of the interactions between the shell and core polymers, but the effect of viscosity differences of the shell polymers cannot be discounted out of hand. Incomplete filling of the printed object to leave voids has been used to explain differences in mechanical properties.[45] However, prior work on core–shell printed materials has shown a significant reduction in the void fraction when there is a large difference in the solidification temperature of the shell and core, even in cases where the viscosity of the shell is greater than iPP,[25] so it is unexpected that there will be significant differences in the void fraction with the iPP *vs.* miPP shell. At low strain, the elastic response is dominated by the PC fibers that extend through the material, but at high strain the adhesion between the core and shell will be important to the mechanical response as the shell is more ductile while PC provides a rigid component. PC and iPP are immiscible, which provide low adhesion. The maleation of PP provides some favorable polar interactions between PC and miPP as well as the potential for grafting[34] to increase the adhesion strength between the core and shell. However, the limited extent of maleation (1%) reduces the probability of these interactions and large differences in the mechanical structure were not expected.

For the stand-on orientation (Fig. 6b), there is a marked decrease in the strength of the printed sample for both core–shell materials. Even for single component filaments, the mechanical properties in this print orientation tend to be inferior since the stress is applied almost exclusively through the interfaces between printed beads.[2,15,46] This orientation is

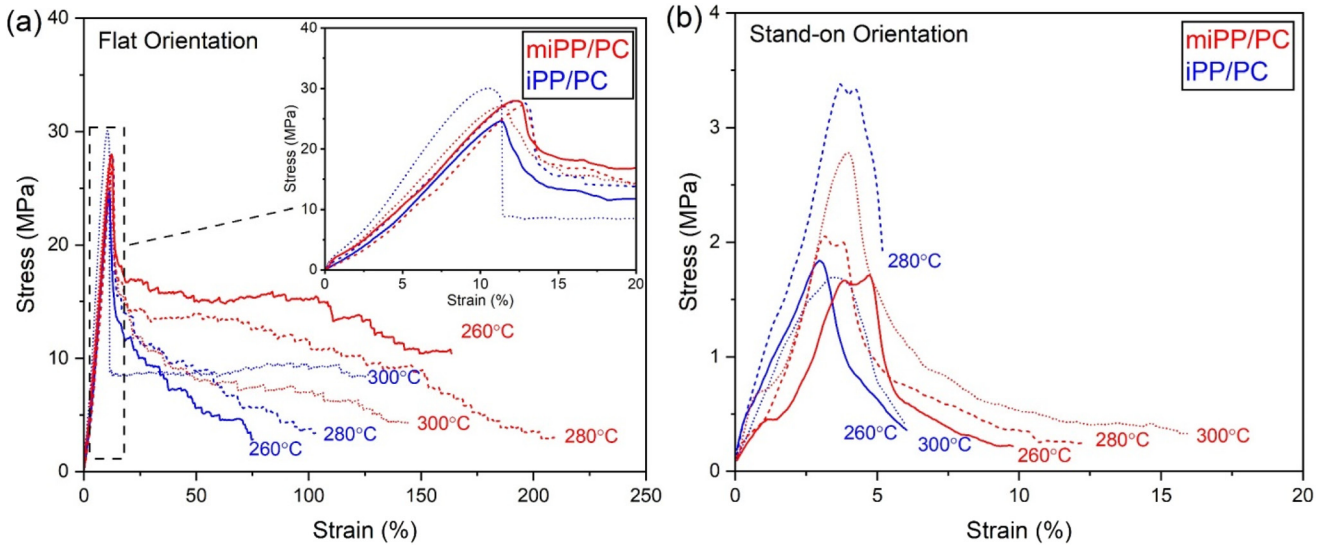

Fig. 6 Representative stress–strain curves of iPP/PC and miPP/PC 3D printed in (a) flat and (b) stand-on orientations as a function of temperature.

effectively all welds, which due to the kinetics of welding and the thermal history of 3D printing tends to be relatively weak.[6] However in this case, the decreased strength can be rationalized by considering these printed objects as fiber composites. In the flat orientation, the stronger PC core fibers are aligned in the direction of the force to effectively carry the applied load, similar to designs that use continuous fiber composites.[47] In the stand-on orientation, the PC fibers are perpendicular to the applied force and thus cannot carry the stress. Unlike most plastics printed in the stand-on build orientation, the failure of the printed parts does not occur at the bead–bead interface, but rather within a bead with the PC core remaining intact on one of the fracture surfaces. This behavior has previously been observed for other immiscible polymer pairs with core–shell filaments when printed in the stand-on orientation.[25] The PP matrix, which is significantly weaker than PC (see Fig. S10 and S11†), controls the stress–strain response. As the PC fibers align perpendicular to the tensile direction, these could effectively work as defects in the sample to promote the growth of cracks. We attribute the increased strain at break for the miPP/PC specimens to the improved adhesion of miPP to PC which reduces the probability of catastrophic failure at this interface. Images of the specimens after failure are shown in Fig. S12.†

Fig. 7 summarizes the mechanical properties of the printed objects. The elastic modulus of 3D printed parts is the most common mechanical metric to describe their performance.[9,48] Due to the printing temperatures being defined by the higher T_g of the PC core of the filament, the effect of the print temperature on Young's modulus is small as shown in Fig. 6a. Similarly, the selection of the shell (iPP *vs.* miPP) did not significantly impact the Young's modulus of the printed parts. However, the print orientation had a significant impact on Young's modulus. This can be rationalized in terms of con-

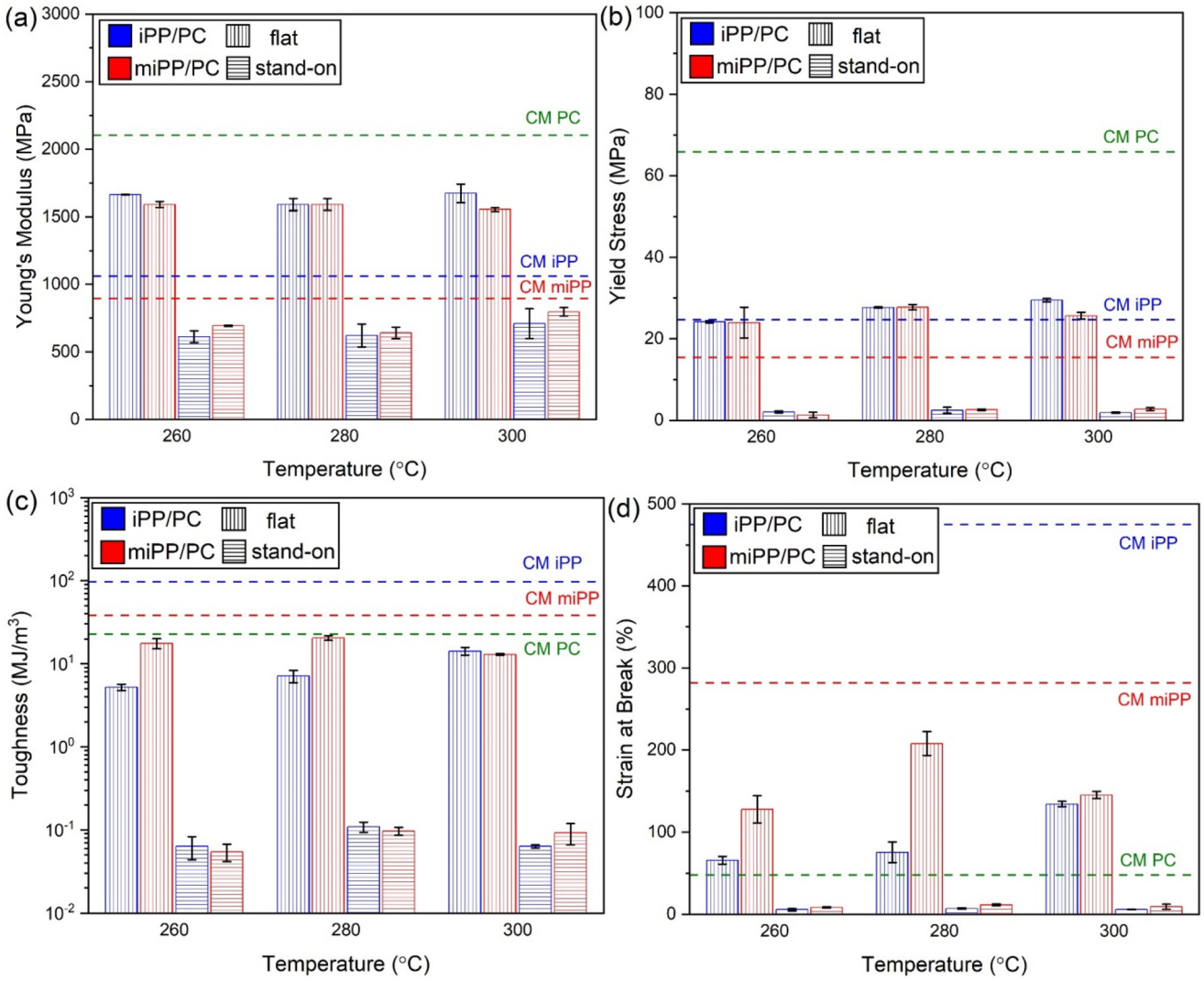

Fig. 7 (a) Elastic modulus, (b) yield stress, (c) toughness, and (d) strain at break from the tensile measurements for the 3D printed core–shell materials. The dashed horizontal lines correspond to the properties of the compression molded polymers as a reference.

tinuous fiber composite theory.[49] For the tensile specimens printed in the flat orientation, there are 7 layers of beads that are deposited in an alternating 0° and 90° orientation relative to the elongation direction. Using this composite theory, the predicted elastic modulus of the flat orientation is 1465 MPa for iPP/PC and 1418 MPa for miPP/PC based on the measured properties of the individual components with compression molding (horizontal lines in Fig. 7a). These predicted values agree well with the properties obtained with the core shell filaments, which suggests that there are only limited voids in the printed objects and the difference in viscosity between miPP and iPP are not responsible for the differences in mechanical performance. The actual values are higher than the prediction due to the printed perimeter being effectively aligned at 0° for all layers. In contrast, the PC fibers do not extend in the elongation direction when printed in the stand-on orientation. Thus, the weaker continuous PP phase deforms under the load around the stiff PC fibers. The load bearing capabilities of the PC fibers that run perpendicular to the applied stress are dependent on their coupling with the continuous PP phase. As the adhesion between PP and PC is not expected to be high, the PC effectively acts as a defect to mostly reduce the effective area supporting the load, which is consistent with the modulus of the printed stand-on specimens being lower than the compression molded iPP or miPP. This poor adhesion between PP and PC is consistent with attempts at lap shear joints, which failed upon handling the polymers used in the core–shell filaments examined (Fig. S13†). Despite the lower modulus of miPP, the stand-on printed specimen using miPP tends to exhibit a higher modulus in the stand-on build orientation. This is likely associated with the improved adhesion of the polypropylene matrix to the PC core to increase the ability of the PC core fibers that are perpendicular to the applied stress to hold some of the load.

In addition to the elastic modulus, the yield stress of the printed parts provides another key metric to describe the mechanical performance of these core–shell materials as shown in Fig. 7b. Similar to Young's modulus, the yield stress is not strongly dependent on the extrusion temperature or selection of the shell PP. The build orientation is however strongly coupled to the yield stress, which can be rationalized in the same manner as Young's modulus in terms of the PC forming fibers within the printed part that act like a composite material. However, the yield stress for the flat orientation is not appreciably greater than those of pure PP materials. The ability to withstand an applied load is significantly less when printed in the stand-on orientation, which is likely associated with the PC fibers effectively acting as defects.

The toughness of the specimens was determined from the area under the stress–strain curve prior to failure. As shown in Fig. 7c, the miPP shell tends to lead to enhanced toughness at lower temperatures when printed in the flat build orientation, while the toughness is statistically independent of shell PP selection for extrusion at 300 °C. There is more than an order of magnitude reduction in the toughness of the printed materials when comparing the two build orientations. This is a result of two factors: the decreased Young's modulus (Fig. 6a) and the reduced elongation at break (Fig. 7d). The failure for the flat build orientation occurs at strains between that of pure PC and PP, while the failure occurs at lower strains with the stand-on orientation. This inferior strain performance with the stand-on orientation is consistent with the PC fibers acting essentially as defects where a crack can readily propagate along the PC/PP interface. In general, the miPP shell leads to 3D printed parts with a higher strain at break in both build orientations. This behavior suggests that the adhesion of miPP to PC is better than that of iPP to PC.

To better understand the differences, the fracture area of the tensile bars was examined with optical microscopy. Fig. 8 illustrates the differences in the morphology of the failure based on the shell (iPP *vs.* miPP) and build orientation (flat *vs.* stand-on) at an extrusion temperature of 280 °C. Additional micrographs for other temperatures are shown in Fig. S14 and S15.† Samples printed in the flat build orientation have continuous lines of the core along the deformation direction. The core acts as a long fiber reinforcement with the PC core materials extending beyond where iPP or miPP failed, but the morphology where the matrix failed is dependent on the shell material. For iPP/PC materials, iPP fails in nearly a straight line across the width of the specimen (Fig. 8A). Conversely, the miPP failure is jagged with changes in the angle occurring near the center of a PC core fiber in the specimen. This difference can be explained in terms of the interaction of the matrix polymer with the core fibers. With iPP and PC, iPP is non-polar with alkyl units (CH, CH_2 and CH_3) that can only act through van der Waals interactions with PC, which contains polar components within the monomer repeat. Without specific favorable interactions between the highly non-polar iPP and PC, the matrix can fail around the fibers and there is nothing to blunt or slow the crack tip. miPP adds a small fraction (1%) of a polar moiety that has the potential to crosslink with any hydroxyl end groups on PC. The polar interactions between maleic anhydride in miPP and the carbonyl in PC will increase the energy to separate the core PC from the shell miPC. This interaction will increase the force required to separate the matrix polymer from the PC fiber but the low functionalization of miPP likely produces heterogeneity in the local force required for separation and thus cracks will not propagate straight across the specimen. These are consistent with the higher toughness of miPP/PC at 280 °C (Fig. 7c). Conversely, the failure of specimens printed in the stand-on build orientation is a nearly clean fracture across the width. The failure surface is nearly parallel to the printed line with iPP/PC with a small deformation of some fibers near the fracture surface (Fig. 8C), while there is some additional deformation near the fracture with miPP/PC (Fig. 8D). This difference could result from the improved coupling between miPP and PC that allows for the stress near the initial crack to spread over a larger area to deform the fracture surface; this mechanism could modestly increase the strain at break (Fig. 7D), but this change does not appear to be statistically significant.

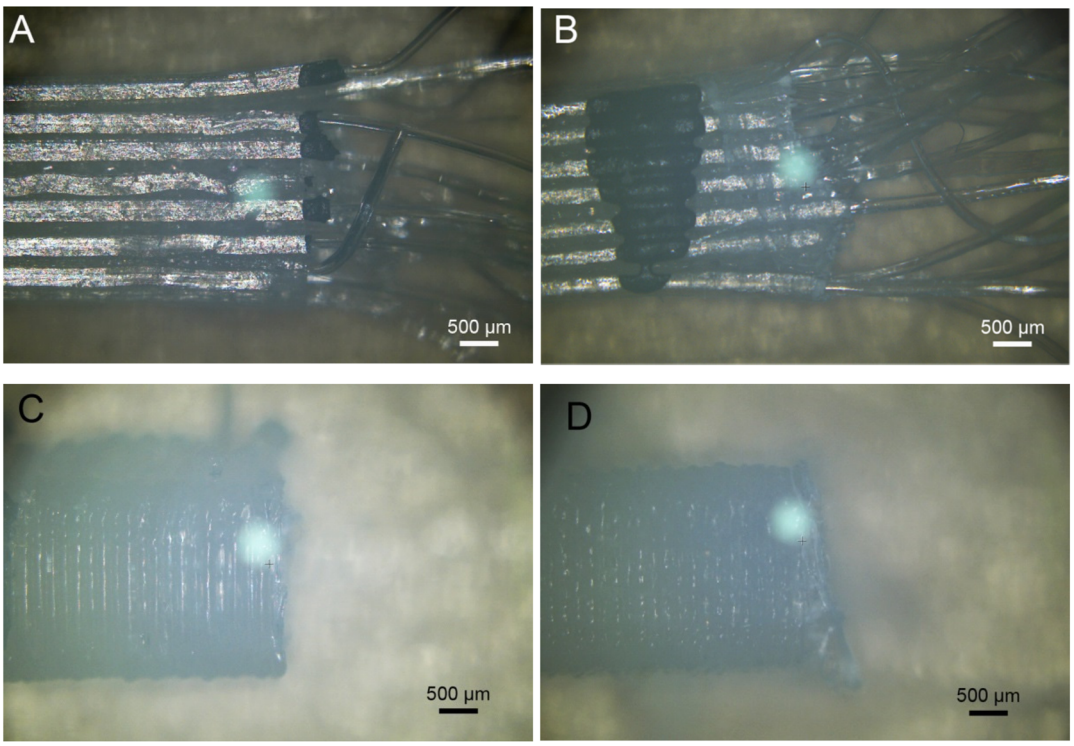

Fig. 8 Optical micrographs illustrating the top down view of the fracture surfaces for tensile specimens printed at 280 °C for (A) iPP-PC in the flat orientation, (B) miPP-PC in the flat orientation, (C) iPP-PC in the stand-on orientation and (D) miPP-PC in the stand-on orientation.

To better understand the differences in the interfacial interactions with PC that are suggested by the fracture images and mechanical behavior, a ball-on-flat reciprocating tribometer was used to quantify the coefficient of friction (COF) between a PC ball and a flat PP sheet. Based on the modulus of each material (Fig. S7a†), the nominal Hertzian contact pressure, deformation, and diameter are estimated to be 27–29 MPa, 5.4–5.9 μm, 90–94 μm, respectively. Fig. 9 illustrates the difference in the COF. The surface roughness is similar between miPP and iPP as shown in Fig. S16.† The higher COF for the PC-on-miPP pair than the PC-on-iPP pair is indicative of stronger interactions between PC and miPP as a result of maleation. The higher COF must be due to the enhanced interfacial interactions which could originate from chain entanglements at the sliding interface through grafting of PC to the maleic anhydride in miPP or simply due to stronger interactions between polar groups (maleate in miPP and carbonate in PC).[50,51] Due to the glassy nature of PC, the low maleation extent (1%), and the reported reaction kinetics for reactions of maleic anhydrides with –OH,[52] it is unlikely that the increase in friction is due to chain entanglements at the sliding interface. In any case, the difference in the COF is consistent with the observed mechanical behavior of the core–shell filaments. It should be noted that the adhesion between the PC and PP is weak as indicated by the failure of lap shear specimens prior to testing. Nonetheless, the minor improvement in the adhesion between the core and shell with maleation leads to primary improvements in the extension at break. Along with the COF result,

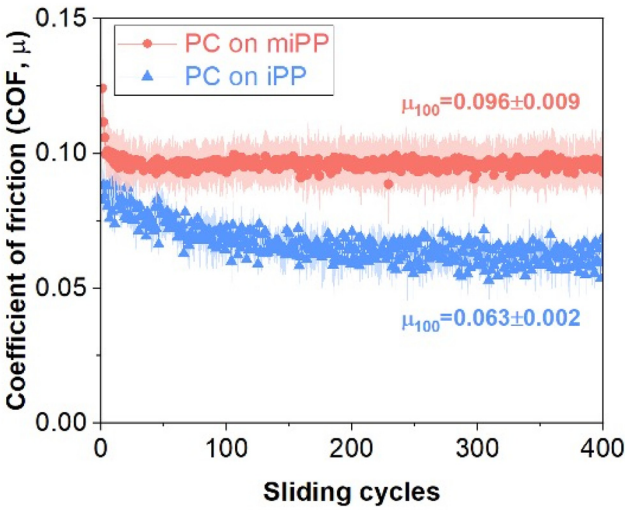

Fig. 9 Coefficient of friction measured from tribo-tests using spherical PC balls on flat iPP or miPP surfaces. The shaded areas show the standard deviation of the data, calculated from three independent measurements.

these indicate that some 'enhanced' interfacial interaction, likely through polarity, between the core and shell materials is beneficial for the overall mechanical response. The use of partially miscible polymer pairs (PC and ABS) in structured filaments has been shown to lead to improved mechanical pro-

perties for the stand-on orientation through post-process annealing at a temperature between the T_g values of the two polymers,[15] but the strength of the 3D printed part remains less than that of the injection molded ABS. Prior work with core–shell filaments suggested that poor adhesion between the core and shell polymers could be beneficial for impact energy dissipation when printed in the flat or edge-on build orientation.[25] Further investigations are needed to better understand how the adhesion between the components in structured filaments influences the mechanical properties of 3D printed parts, but this work does illustrate the potential advantages of improving the adhesion between the polymeric components.

Conclusions

The role of interfacial interactions in core–shell filaments in the characteristics of printed parts from the perspective of both mechanical performance and dimensional accuracy is investigated. Immiscible polymer pairs of polypropylene (PP) and polycarbonate (PC) were examined, but maleation of PP provides improved favorable polar interactions between PP and PC as evidenced by a 50% increase in the sliding friction. miPP as the shell leads to increases in the ductility of the printed parts using core–shell filaments, despite the decreased extensibility of miPP in comparison with iPP for the individual components. Despite printing at a higher temperature than typical of PP, the printed structures were close in dimensional accuracy to the brittle PC except in the case of small holes where the miPP/PC filaments performed poorly due to volume expansion upon melting of the PP crystals, low surface tension and high melt mobility. The surface finish as probed by optical profilometry is only modestly impacted by the increased mobility of the shell polymer, presumably due to surface tension effects and limited time for flow during the print. These results demonstrate that the interactions within multi-polymer systems for MEAM present an additional handle to enhance the mechanical performance of 3D printed plastics.

Conflicts of interest

There are no conflicts to declare.

Acknowledgements

This work was financially partially supported by the National Science Foundation (grant CMMI-2011289). Polycarbonate materials were supplied by Covestro LLC (Pittsburgh PA). The authors acknowledge the use of the Penn State Materials Characterization Lab for tensile measurements. The tribotesting was done with the support from the NSF (Grant No: CMMI-1912199). WF acknowledges the support from an undergraduate research internship through the National Aeronautics and Space Administration under Grant No. 80NSSC20M0097 issued through the Pennsylvania Space Grant Consortium. The authors thank Yun Zhu for his assistance with obtaining optical micrographs of the fractured samples, Po-Hao Lai for his assistance with FTIR and Sierra Yost for her help with rheology.

References

1 A. Das, C. A. Chatham, J. J. Fallon, C. E. Zawaski, E. L. Gilmer, C. B. Williams and M. J. Bortner, *Addit. Manuf.*, 2020, **34**, 101218.
2 A. Cano-Vicent, M. M. Tambuwala, S. S. Hassan, D. Barh, A. A. A. Aljabali, M. Birkett, A. Arjunan and A. Serrano-Aroca, *Addit. Manuf.*, 2021, **47**, 102378.
3 M. Pagac, J. Hajnys, Q. P. Ma, L. Jancar, J. Jansa, P. Stefek and J. Mesicek, *Polymers*, 2021, **13**, 598.
4 A. Marzola, E. Mussi and F. Uccheddu, *Design Tools and Methods in Industrial Engineering, ADM*, 2019, vol. 2020, pp. 936–947.
5 E. L. Gilmer, D. Anderegg, J. M. Gardner, G. Sauti, E. J. Siochi, S. H. McKnight, D. A. Dillard, C. McIlroy and M. J. Bortner, *Addit. Manuf.*, 2021, **48**, 102412.
6 S. C. Perryman and M. D. Dadmun, *Addit. Manuf.*, 2021, **38**, 101746.
7 T. J. Coogan and D. O. Kazmer, *Addit. Manuf.*, 2020, **35**, 101368.
8 A. Costanzo, R. Spotorno, M. V. Candal, M. M. Fernandez, A. J. Mueller, R. S. Graham, D. Cavallo and C. McIlroy, *Addit. Manuf.*, 2020, **36**, 101415.
9 A. El Magri, K. El Mabrouk, S. Vaudreuil, H. Chibane and M. E. Touhami, *J. Appl. Polym. Sci.*, 2020, **137**, 49087.
10 W. Gao, Y. B. Zhang, D. Ramanujan, K. Ramani, Y. Chen, C. B. Williams, C. C. L. Wang, Y. C. Shin, S. Zhang and P. D. Zavattieri, *Comput. Aided Des.*, 2015, **69**, 65–89.
11 J. R. C. Dizon, C. C. L. Gache, H. M. S. Cascolan, L. T. Cancino and R. C. Advincula, *Technologies*, 2021, **9**, 61.
12 F. Tamburrino, S. Barone, A. Paoli and A. V. Razionale, *Virtual Phys. Prototyp.*, 2021, **16**, 218–251.
13 C. Basgul, T. Yu, D. W. MacDonald, R. Siskey, M. Marcolongo and S. M. Kurtz, *J. Mech. Behav. Biomed. Mater.*, 2020, **102**, 103455.
14 K. R. Hart, R. M. Dunn, J. M. Sietins, C. M. H. Mock, M. E. Mackay and E. D. Wetzel, *Polymer*, 2018, **144**, 192–204.
15 B. Koker, R. Ruckdashel, H. Abajorga, N. Curcuru, M. Pugatch, R. Dunn, D. O. Kazmer, E. D. Wetzel and J. H. Park, *Addit. Manuf.*, 2022, **55**, 102807.
16 A. El Magri, K. El Mabrouk, S. Vaudreuil and M. E. Touhami, *J. Appl. Polym. Sci.*, 2021, **138**, 49625.
17 C. B. Sweeney, B. A. Lackey, M. J. Pospisil, T. C. Achee, V. K. Hicks, A. G. Moran, B. R. Teipel, M. A. Saed and M. J. Green, *Sci. Adv.*, 2017, **3**, e1700262.
18 J. Bartolai, T. W. Simpson and R. X. Xie, *Rapid Prototyp. J.*, 2018, **24**, 321–332.

19 D. P. Street, W. K. Ledford, A. A. Allison, S. Patterson, D. L. Pickel, B. S. Lokitz, J. M. Messman and S. M. Kilbey, *Macromolecules*, 2019, **52**, 5574–5582.
20 S. Rose, A. Prevoteau, P. Elziere, D. Hourdet, A. Marcellan and L. Leibler, *Nature*, 2014, **505**, 382–385.
21 Z. B. Xiao, Q. X. Zhao, Y. W. Niu and D. Zhao, *Soft Matter*, 2022, **18**, 3447–3464.
22 D. P. Street, A. H. Mah, W. K. Ledford, S. Patterson, J. A. Bergman, B. S. Lokitz, D. L. Pickel, J. M. Messman, G. E. Stein and S. M. Kilbey, *ACS Appl. Polym. Mater.*, 2020, **2**, 1312–1324.
23 J. R. Ai, F. Peng, P. Joo and B. D. Vogt, *ACS Appl. Polym. Mater.*, 2021, **3**, 2518–2528.
24 F. Peng, H. W. Jiang, A. Woods, P. Joo, E. J. Amis, N. S. Zacharia and B. D. Vogt, *ACS Appl. Polym. Mater.*, 2019, **1**, 275–285.
25 F. Peng, Z. Y. Zhao, X. H. Xia, M. Cakmak and B. D. Vogt, *ACS Appl. Mater. Interfaces*, 2018, **10**, 16087–16094.
26 A. Sover, V. Ermolai, A. M. Raichur, R. Ciobanu, M. Aradoaei and N. Lucanu, *Polymers*, 2021, **13**, 4253.
27 K. R. Hart, R. M. Dunn and E. D. Wetzel, *Adv. Eng. Mater.*, 2020, **22**, 1901184.
28 A. Naqi, Z. Swain and M. E. Mackay, *ACS Appl. Polym. Mater.*, 2023, **5**, 2481–2489.
29 J. Lee, R. Ruckdashel, N. Patil, M. Pugatch, K. Joshi and J. H. Park, *ACS Appl. Polym. Mater.*, 2023, **5**, 2867–2876.
30 H. Narei, M. Fatehifar, A. H. Malt, J. Bissell, M. Souri, M. N. Esfahani and M. Jabbari, *Polymers*, 2021, **13**, 476.
31 Z. C. Kennedy and J. F. Christ, *Addit. Manuf.*, 2020, **36**, 101233.
32 Z. Z. Yu, Y. C. Ou and G. H. Hu, *J. Appl. Polym. Sci.*, 1998, **69**, 1711–1718.
33 R. J. M. Borggreve and R. J. Gaymans, *Polymer*, 1989, **30**, 63–70.
34 S. A. Madbouly, J. U. Otaigbe and T. Ougizawa, *Macromol. Chem. Phys.*, 2006, **207**, 1233–1243.
35 A. Ait-Kadi, M. Bousmina, A. A. Yousefi and F. Mighri, *Polym. Eng. Sci.*, 2007, **47**, 1114–1121.
36 S. H. P. Bettini and J. A. M. Agnelli, *Polym. Test.*, 2000, **19**, 3–15.
37 J. R. Ai and B. D. Vogt, *Prog. Addit. Manuf.*, 2022, 1009–1021.
38 Q. L. Ni, J. Q. Fan, H. Niu and J. Y. Dong, *J. Appl. Polym. Sci.*, 2011, **121**, 2512–2517.
39 S. F. Yost, C. W. Pester and B. D. Vogt, *J. Polym. Sci.*, 2024, DOI: **10.1002/pol.20230559**, in press.
40 M. Spoerk, C. Holzer and J. Gonzalez-Gutierrez, *J. Appl. Polym. Sci.*, 2020, **137**, 48545.
41 N. Vidakis, M. Petousis, E. Velidakis, L. Tzounis, N. Mountakis, J. Kechagias and S. Grammatikos, *Materials*, 2021, **14**, 3076.
42 A. Das, A. E. C. Marnot, J. J. Fallon, S. M. Martin, E. G. Joseph and M. J. Bortner, *ACS Appl. Polym. Mater.*, 2020, **2**, 911–921.
43 D. Stoof and K. Pickering, *Composites, Part B*, 2018, **135**, 110–118.
44 C. Tzoganakis, J. Vlachopoulos and A. E. Hamielec, *Polym. Eng. Sci.*, 1988, **28**, 170–180.
45 X. C. Sun, M. Mazur and C. T. Cheng, *Addit. Manuf.*, 2023, **67**, 103463.
46 J. L. Hor, Y. J. Jiang, D. J. Ring, R. A. Riggleman, K. T. Turner and D. Lee, *ACS Nano*, 2017, **11**, 3229–3236.
47 S. M. F. Kabir, K. Mathur and A. F. M. Seyam, *Compos. Struct.*, 2020, **232**, 111476.
48 A. A. Bakir, R. Atik and S. Ozerinc, *J. Appl. Polym. Sci.*, 2021, **138**, 49709.
49 E. Jacquet, F. Trivaudey and D. Varchon, *Compos. Sci. Technol.*, 2000, **60**, 345–350.
50 J. Klein, *Annu. Rev. Mater. Sci.*, 1996, **26**, 581–612.
51 M. Leolukman and S. H. Kim, *Langmuir*, 2005, **21**, 682–685.
52 M. A. J. Van der Mee, J. G. P. Goossens and M. Van Duin, *J. Polym. Sci., Part A: Polym. Chem.*, 2008, **46**, 1810–1825.